MULTISCALE MODELING AND SIMULATION OF A CAHN–LARCHÉ SYSTEM WITH PHASE SEPARATION ON THE MICROSCALE*

L. REISCHMANN† AND M. A. PETER‡

Abstract. We consider the process of phase separation of a binary system under the influence of mechanical stress and we derive a mathematical multiscale model, which describes an evolving microstructure taking into account the elastic properties of the involved materials. Motivated by phase-separation processes observed in lipid monolayers in film-balance experiments, the starting point of the model is the Cahn–Hilliard equation coupled with the equations of linear elasticity, the so-called Cahn–Larché system. Owing to the fact that the mechanical deformation takes place on a macrosopic scale whereas the phase separation happens on a microscopic level, a multiscale approach is imperative. We assume the pattern of the evolving microstructure to have an intrinsic length scale associated with it, which, after nondimensionalization, leads to a scaled model involving a small parameter $\epsilon > 0$, which is suitable for periodic-homogenization techniques. The problem is formally homogenized using the method of two-scale asymptotic expansions, which leads to a model of distributed-microstructure type in the limit. Finally, numerical simulations based on finite elements showcase the model behavior of the distributed-microstructure model.

Key words. Cahn–Larché system, distributed-microstructure model, periodic homogenization, asymptotic expansion, phase separation

AMS subject classifications. 35B27, 74Q10, 35B36, 74N15

DOI. 10.1137/20M1321103

1. Introduction.

Binary phase-separation processes are often described by the Cahn–Hilliard equation, a fourth-order equation for an order parameter taking different distinct values in each of the two phases; see the recent monograph [22] for example. It is derived from a free-energy potential and ensures mass conservation. The Cahn–Larché system is the result of coupling the Cahn–Hilliard equation with the equations of linear elasticity in order to take into account mechanical effects in the separation process [16]. The chemical potential of the Cahn–Hilliard equation is extended by a contribution derived from the elastic energy density and the elasticity tensor depends naturally on the order parameter.

In the classical Cahn–Larché system, all processes are modeled on the same length scale. However, in certain situations, the phase separation and the mechanics occur on distinctly different scales, which requires a multiscale analysis of the Cahn–Larché system. This can be achieved in a homogenization context by the method of asymptotic expansion and it is the focus of this work.

This study is motivated by the process of phase separation in lipid monolayers, which can be observed in film-balance experiments, where phospholipid monolayers are compressed. Such monolayers are investigated in experiments since phosphatidylcholines are the main phospholipids found in mammalian cell membranes. The lipid dipalmitoylphosphatidylcholine (DPPC) is particularly common in this con-

*Received by the editors February 24, 2020; accepted for publication (in revised form) June 19, 2020; published electronically September 23, 2020.

https://doi.org/10.1137/20M1321103

†Institute of Mathematics, University of Augsburg, 86135 Augsburg, Germany (lisa.reischmann@math.uni-augsburg.de).

‡Institute of Mathematics, University of Augsburg, 86135 Augsburg, Germany and Augsburg Centre for Innovative Technologies, University of Augsburg, 86135 Augsburg, Germany (malte.peter@math.uni-augsburg.de, https://appa.math.uni-augsburg.de/).

text (see, e.g., [13, 18, 25]), but many other phosphatidylcholines and, more generally, other phospholipids are used, such as DMPC, DMPG, DMPE, DOPC, DLPC (see, e.g., [21, 23, 14]). Biomembranes actually have the structure of a bilayer, but monolayers, which provide a simplified experimental model of such membranes, have the advantage of simplified production and, in addition, the molecular density of a monolayer can be controlled by varying the area per molecule on a Langmuir–Blodgett film balance [18]. A film balance is essentially a kind of water trough, equipped with a controllable teflon barrier and a fluorescence microscope. The total area of the lipid monolayer and consequently the density of the molecules can be controlled by moving the barrier.

Lipids show different states or phases, corresponding to the alignment of the lipid molecules, depending on certain factors. Generally, the lipids in the monolayer align themselves with their hydrophilic head groups in the direction of the water due to their amphiphilic properties. Assuming constant temperature, the monolayer becomes denser and more rigid as the area available for the lipid monolayer is reduced, which corresponds to increasing the lateral pressure. In the liquid-expanded (LE) phase, the molecules are disordered and the chains are partially of convoluted structure. In the liquid condensed (LC) phase, the molecules are much more closely packed and ordered. After spreading the lipid mixture on the film balance, the lipid molecules initially have plenty of space and are in a state known as the gas-analogue phase. If the space available to the molecules is then reduced, a phase transition occurs in which parts of the monolayer are transferred into the LE phase until, with further compression, the entire monolayer is present in the LE phase. Further compression results in a further phase transition into the LC phase. This part is the motivation of this work: In experiments, the formation of two-phase regions can be observed in which regions in the LC phase are dispersed in the less ordered LE phase. The size of the LC domains is in the range of several microns, which differs from the scale of the mechanical deformation induced by the teflon barrier by approximately 5 orders of magnitude. The mechanical processes influence the size and shape of the arising domains such as speed and strength of compression or waiting periods during multiple compression operations, [18, 13, 25].

By interpreting the lipid monolayer with its coexisting phases as a binary mixture, we use the Cahn–Hilliard model, which has already been successfully adapted to study phase-separation processes in lipid bilayers [4, 8], to describe the phase separation. In the context of phase separation in lipid monolayers, the Cahn–Hilliard model has already been extended to take elastic effects into account. In [3], it was coupled with a viscoelastic fluid-flow model to study phase-separation processes in lipid monolayers for a surface-acoustic-wave-actuated fluid flow for a monolayer in a fluidic regime. Here, we consider the further compressed state. Since the LC phase of the monolayer is gel-like and has an already relatively densely packed and ordered molecular structure, we interpret the monolayer as a solid and use solid mechanics to describe the mechanical behavior of the monolayer mathematically.

Motivated by these film-balance experiments, in what follows, we generally consider a separation process in a binary solid under the influence of mechanical stress, where the mechanical deformation takes place on a macroscopic scale and the phase separation happens on a microscopic scale, and we use the Cahn–Larché system to model this phenomenon. We note that a (viscoelastic) Cahn–Larché model in a multiscale context was used to study the decomposition process in eutectic alloys in [20].

In section 2, we introduce the Cahn–Larché system and discuss it in the film-balance context. In order to obtain a process-adapted model, in section 3 we pres-

ent a nondimensionalization, which leads to a scaled system where different involved characteristic length scales are taken into account and which is suitable for periodic-homogenization techniques. This system is formally homogenized in section 4 via two-scale asymptotic expansions. The resulting system is of the so-called distributed-microstructure type which, in the limit, is a typical result for coupled systems where one process occurs on the macroscopic scale and the other one on the microscopic scale. Finally, in section 5, numerical simulations based on finite elements are presented to showcase the model behavior.

2. The Cahn–Larché system. We briefly recall the Cahn–Hilliard model and its extension to the Cahn–Larché model in our notation. For the Cahn–Hilliard model, we define an order parameter $c\colon \Omega \times (0,T) \to [0,1]$, which describes the relative concentration of a binary mixture in a domain $\Omega \subset \mathbb{R}^N$ with boundary $\Gamma = \partial\Omega$ over the time interval $(0,T)$, where $T > 0$. Pure phases of the components correspond to $c = 0$ and $c = 1$. We introduce a local free energy density (per volume) f so that the total free energy of the mixture can be defined by

$$\int_\Omega f(c) + \frac{\lambda}{2}|\nabla c|^2 \,\mathrm{d}x. \tag{2.1}$$

The second term is a regularization term, which penalizes interfaces. The parameter λ can be interpreted as related to a line tension (in two dimensions). Specifically, we choose a double-well potential of the form

$$f(c) = \varphi c^2(1-c)^2, \tag{2.2}$$

with a scaling parameter $\varphi > 0$. The minimas of the double-well potential are achieved for $c = 0$ and $c = 1$, i.e., for pure phases. For homogeneous mixtures, the local free energy is greater. Therefore, it is the driving force for phase separation of a homogeneous mixture.

To arrive at a closed system, we introduce the chemical potential μ^{CH}, which can be defined via the first variation of the total free energy with respect to c, i.e.,

$$\mu^{\mathrm{CH}} = f'(c) + \lambda\Delta c. \tag{2.3}$$

According to Fick's law of diffusion, the mass flow is given by

$$j = -M\nabla\mu^{\mathrm{CH}}, \tag{2.4}$$

where M denotes the mobility. Conservation of mass leads to an evolution equation for the relative concentration c,

$$\partial_t c = \nabla\cdot(M\nabla\mu^{\mathrm{CH}}). \tag{2.5}$$

Inserting now the chemical potential defined by (2.3), we obtain the Cahn–Hilliard equation, which describes the change of the relative concentration in time in a given domain Ω,

$$\partial_t c = \nabla\cdot\big(M\nabla\big(f'(c) - \lambda\Delta c\big)\big). \tag{2.6}$$

For future reference, we note that, according to [15], we choose a constant mobility factor of the form

$$M = \varphi_*^{-1} D, \tag{2.7}$$

where the dimensional factor φ_* denotes a characteristic value of the free energy of the system.

The Cahn–Hilliard model does not capture effects caused by mechanical deformations. This can be achieved by including an elastic contribution in the free energy, which is the Cahn–Larché model introduced in [16]. If only small deformations are considered, a linearized theory is applicable. Thus, we consider only infinitesimal strains defined by the linear strain tensor

$$\mathcal{E}(u) = \frac{1}{2}\left(\nabla u + (\nabla u)^{\mathrm{T}}\right), \tag{2.8}$$

where $u\colon \Omega \times (0,T) \to \mathbb{R}^N$ is the deformation field. Typically, the two phases have different elastic properties. Thus, the elasticity tensor $\mathcal{A}(c)$, which contains the material parameters characterizing the stiffness of the phases, naturally depends on the order parameter c. According to Hooke's law, the stress tensor is defined by

$$\mathcal{S} = \mathcal{A}(c)\big(\mathcal{E}(u) - \bar{\mathcal{E}}(c)\big), \tag{2.9}$$

where $\bar{\mathcal{E}}(c)$ denotes the eigenstrain. In general, this refers to a strain which is present in the absence of any applied stress. This phenomenon occurs in the presence of inhomogeneities, such as thermal expansions with phase transitions and leads to self-generated internal stress [24]. The eigenstrain is often referred to as stress-free strain and, just like the elastic material parameters, it may be different for each phase. A natural choice is a multiple of the identity

$$\bar{\mathcal{E}}(c) = e(c)\mathbb{1}, \tag{2.10}$$

where the scalar-valued function e specifies the eigenstrain behavior at a particular phase state and $\mathbb{1} \in \mathbb{R}^{N\times N}$ is the second-order identity tensor. So, according to (2.10), the eigenstrain is uniform in all directions, which seems to be a common choice; see, e.g., [24, 7, 36]. According to [6, 12] the elastic energy density is now given by

$$\mathcal{W}(u,c) = \frac{1}{2}(\mathcal{E}(u) - \bar{\mathcal{E}}(c)) : \mathcal{A}(c)\,(\mathcal{E}(u) - \bar{\mathcal{E}}(c)). \tag{2.11}$$

Adding the contribution of the elastic energy density (2.11) to (2.1), the total energy of the system is given by

$$\int_\Omega f(c) + \frac{\lambda}{2}|\nabla c|^2 + \mathcal{W}(u,c)\,\mathrm{d}x \tag{2.12}$$

and the chemical potential (2.3) of the system extends to

$$\mu = f'(c) - \lambda\Delta c - \bar{\mathcal{E}}'(c) : \mathcal{S} + \frac{1}{2}(\mathcal{E}(u) - \bar{\mathcal{E}}(c)) : \mathcal{A}'(c)(\mathcal{E}(u) - \bar{\mathcal{E}}(c)). \tag{2.13}$$

Inserting (2.13) into (2.5) leads to an extended Cahn–Hilliard equation,

$$\partial_t c = \nabla\cdot\Big(M\nabla\left(f'(c) - \lambda\Delta c - \bar{\mathcal{E}}'(c) : \mathcal{S} + \frac{1}{2}(\mathcal{E}(u) - \bar{\mathcal{E}}(c)) : \mathcal{A}'(c)(\mathcal{E}(u) - \bar{\mathcal{E}}(c))\right)\Big). \tag{2.14}$$

This equations needs to be supplemented by an equation of conservation of momentum, which, taking into account (2.9), is given by

$$\varrho\partial_t^2 u = \nabla\cdot\mathcal{S} = \nabla\cdot\big(\mathcal{A}(c)(\mathcal{E}(u) - \bar{\mathcal{E}}(c))\big), \tag{2.15}$$

where ϱ is the density and neglecting gravitational effects. If we use our representation for the eigenstrain (2.10), then, since

$$\bar{\mathcal{E}}'(c) : \mathcal{S} = e'(c)\mathbb{1} : \mathcal{S} = e'(c)\,\mathrm{tr}(\mathcal{S}),$$

we obtain the Cahn–Larché system as follows:

$$\partial_t c = \nabla \cdot \Big(M \nabla \big(f'(c) - \lambda \Delta c - e'(c)\,\mathrm{tr}(\mathcal{S}) + \frac{1}{2}(\mathcal{E}(u) - e(c)\mathbb{1}) : \mathcal{A}'(c)(\mathcal{E}(u) - e(c)\mathbb{1}) \big) \Big) \quad \text{in } \Omega \times (0,T), \tag{2.16a}$$

$$\varrho \partial_t^2 u = \nabla \cdot \Big(\mathcal{A}(c)\big(\mathcal{E}(u) - e(c)\mathbb{1}\big) \Big) \quad \text{in } \Omega \times (0,T). \tag{2.16b}$$

The system is completed by initial conditions for c and u and boundary conditions, typically no-flux conditions for c and μ in order to ensure mass conservation

$$\nabla c \cdot n = 0 \ \text{ on } \Gamma \times S, \quad \nabla \mu \cdot n = 0 \ \text{ on } \Gamma \times S,$$

where n denotes the outer normal vector on Γ, as well as displacement and/or traction conditions for the displacement.

As noted above, the two phases typically have different elastic properties and hence we denote the elasticity tensor describing the elastic properties of the elastically softer phase by $\mathcal{A}^\alpha$ and the elasticity tensor of the elastically stiffer phase by $\mathcal{A}^\beta$. Then, following [36], for the mixture, we consider

$$\mathcal{A}(c) := \mathcal{A}^\alpha + d(c)\left(\mathcal{A}^\beta - \mathcal{A}^\alpha\right), \tag{2.17}$$

an elasticity tensor depending on the relative concentration of the mixture, which is simply an interpolation of the two component tensors. The interpolation function d should be defined such that

$$d(0) = 0, \quad d(1) = 1, \quad d'(0) = 0, \quad d'(1) = 0,$$

hence

$$d(x) = \begin{cases} 0, & x < 0, \\ -2x^3 + 3x^2, & 0 \le x \le 1, \\ 1, & x > 1, \end{cases} \tag{2.18}$$

is an appropriate choice. With this we have also determined that $c = 0$ corresponds to the elastically softer phase and $c = 1$ corresponds to the elastically stiffer phase. We assume positive definiteness for the individual component tensor and the usual symmetry conditions in linear elasticity theory, i.e., for $\mathcal{A}^i = (a^i_{ijkh})_{1 \le i,j,k,h \le N}$, $i \in \{\alpha, \beta\}$, we require

$$a^i_{ijkh} = a^i_{ijhk} = a^i_{jikh} = a^i_{khij}. \tag{2.19}$$

Obviously, the interpolated tensor defined by (2.17) is also positive definite and fulfils the symmetry condition (2.19).

Remark 2.1 (existence of weak solutions). The existence of solutions of the Cahn–Larché model is well known. We refer to [9] in particular, where the author studied phase separation in multicomponent alloys in the presence of elastic interactions and proved the existence of solutions of a mixed formulation of the Cahn–Larché system in a Sobolev-space setting. This solution is shown to be uniquely determined if the elasticity tensor is the same for both phases.

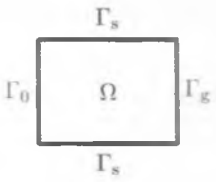

FIG. 1. *Domain Ω with boundary parts Γ_0, Γ_g, and Γ_s.*

Remark 2.2 (film-balance setting). For the modeling of phase separation of lipids in a Langmuir–Blodgett film balance, $\Omega \subset \mathbb{R}^2$ is a rectangular domain representing the area of the water trough of the film balance on which the lipid monolayer is examined, and with boundary $\Gamma_0 \cup \Gamma_g \cup \Gamma_s$, with boundary parts Γ_0, Γ_g, and Γ_s as shown in Figure 1. The force applied by the controllable barrier and by compressing the lipid monolayer is modeled by applying a boundary force g on Γ_g, hence,

$$\mathcal{S}n = g \quad \text{on } \Gamma_g \times S. \tag{2.20}$$

On the opposite boundary part Γ_0 we do not expect any deformation and hence we require

$$u = 0 \quad \text{on } \Gamma_0 \times S. \tag{2.21}$$

Also, the monolayer cannot move beyond the lateral edges in the normal direction. Therefore, on the side part of the boundary Γ_s we set

$$u \cdot n = 0 \quad \text{on } \Gamma_s \times S, \quad n \cdot \mathcal{S}\tau = 0 \quad \text{on } \Gamma_s \times S, \tag{2.22}$$

where τ is the tangential vector on Γ. These conditions describe that the monolayer cannot expand past the lateral edges and does not adhere there when compressed. It would also have been possible to set the free-slip condition on the boundary part Γ_0 as well instead of the Dirichlet condition $u = 0$. However, the boundary condition (2.21) ensures the uniqueness of u.

3. Nondimensionalization and scaling. In section 1, we have already pointed out the multiscale aspect of the considered physical process, which assumes the microstructure of the pattern to have an intrinsic length scale associated with it. The Cahn–Larché system (2.16a), (2.16b) as introduced in section 2 does not take into account that the processes take place on different scales. A suitable scaling of the system, which takes into account the different characteristic lengths, is therefore necessary; see, e.g., [1, 11] for process-adapted scalings of other systems. In our case, this results naturally from a nondimensionalization, similar to, e.g., [26, 29, 28, 27, 19].

To make this more precise, we introduce a characteristic macroscopic length scale L, e.g., representing the order of magnitude of the size of the film balance, and a characteristic microscopic length scale l, which corresponds to the order of magnitude of the scale on which the phase separation is observable, and we write

$$\epsilon = \frac{l}{L} \ll 1. \tag{3.1}$$

It turns out that the nondimensionalization taking into account the characteristic macroscopic length scale L and the characteristic microscopic length scale l results in

a system scaled by powers of ϵ and which is suitable for the application of techniques of periodic homogenization.

To facilitate an asymptotic analysis, the order parameter c, which describes the microstructure, is assumed to depend on two independent spatial variables, x, associated with the macroscale and $\frac{x}{\epsilon}$, associated with the microscale. We denote this with an index ϵ and write

$$c_\epsilon(x,t) = c(x, x/\epsilon, t). \tag{3.2}$$

Note that we achieve this circumstance in practice by choosing an initial value for c_ϵ, depending on the macroscopic variable x and on the microscopic variable $\frac{x}{\epsilon}$. Due to the dependency on the order parameter, this also applies to the elasticity tensor $\mathcal{A}(c_\epsilon)$, which implies an analogue spatial dependence of the displacement field and, hence, we write u_ϵ.

We further define characteristic microscopic lengths associated with the diffusion and the mechanics, l_d and l_m, respectively, and express them as a multiple of the geometric microscopic length l. We choose $l_\mathrm{d} = \frac{1}{10} l$ and $l_\mathrm{m} = l$, since the mechanics happens on the whole microscopic length scale whereas the diffusion scale is typically a little shorter. The characteristic time for the diffusion is then defined by

$$T_\mathrm{d} := \frac{l_\mathrm{d}^r L^{2-r}}{D_\mathrm{ref}}, \tag{3.3}$$

and the characteristic time for the mechanics by

$$T_\mathrm{m} := \left(\frac{l_\mathrm{m}^s L^{2-s} \varrho_\mathrm{ref}}{\sigma_\mathrm{ref}}\right)^{1/2}, \tag{3.4}$$

both depending on powers of the two different characteristic length scales. The respective influence of the different characteristic lengths is regulated by exponents depending on parameters $r, s \in [0,2]$, which we have to determine later. With D_ref, σ_ref, and ϱ_ref we denote reference values corresponding to the diffusivity, the stiffness, and the density, respectively. With the dimensionless macroscopic space variable $\tilde{x} := x/L$ and the time variable $\tilde{t}_\mathrm{d} := t/T_\mathrm{d}$ as well as $D = M\varphi_*$ from (2.7), (2.16a) becomes

$$\begin{aligned}\partial_{\tilde{t}_\mathrm{d}} c_\epsilon = \epsilon^r 10^{-r} \tilde{\Delta} \Big(&\tilde{f}'(c_\epsilon) - \epsilon^2 \tilde{\lambda} \tilde{\Delta} c - e'(c_\epsilon)\,\mathrm{tr}(\tilde{\mathcal{S}}) \\ &+ \frac{1}{2}(\mathcal{E}(u_\epsilon) - e(c_\epsilon)\mathbb{1}) : \tilde{\mathcal{A}}'(c_\epsilon)(\mathcal{E}(u_\epsilon) - e(c_\epsilon)\mathbb{1})\Big),\end{aligned} \tag{3.5}$$

where we have defined the dimensionless quantities as follows:

$$\tilde{f}'(c_\epsilon) := \varphi_*^{-1} f'(c_\epsilon), \quad \tilde{\lambda} := \varphi_*^{-1} \epsilon^{-2} L^{-2} \lambda, \quad \tilde{\mathcal{A}}'(c_\epsilon) := \varphi_*^{-1} \mathcal{A}'(c_\epsilon) \tag{3.6}$$

and

$$\tilde{\mathcal{S}} := \varphi_*^{-1} \mathcal{S} = \varphi_*^{-1} \mathcal{A}(c_\epsilon)(\mathcal{E}(u_\epsilon) - e(c_\epsilon)\mathbb{1}) = \tilde{\mathcal{A}}(c_\epsilon)(\mathcal{E}(u_\epsilon) - e(c_\epsilon)\mathbb{1}) \tag{3.7}$$

with

$$\tilde{\mathcal{A}}(c_\epsilon) := \varphi_*^{-1} \mathcal{A}(c_\epsilon). \tag{3.8}$$

All quantities with a tilde denote dimensionless quantities, where $\tilde{f}'(c_\epsilon)$ is of order 1. Note that the strain is already dimensionless. Further, we have made use of the fact

that the magnitude of the line tension λ is much smaller than the free energy level. In order to account for this and to compensate for the length scale associated with the Laplacian, a factor ϵ^2 is explicitly taken out.

With $\tilde{u} := \frac{u}{L}$ and with the dimensionless time variable $\tilde{t}_{\mathrm{m}} := t/T_{\mathrm{m}}$, (2.16b) becomes

$$\partial_{\tilde{t}_{\mathrm{m}}}^2 \tilde{u}_\epsilon = \epsilon^s \tilde{\nabla} \cdot \big(\tilde{\mathcal{A}}(c_\epsilon)(\mathcal{E}(u_\epsilon) - e(c_\epsilon)\mathbb{1})\big) \tag{3.9}$$

with dimensionless elasticity tensor

$$\tilde{\mathcal{A}}(c_\epsilon) = \sigma_{\mathrm{ref}}^{-1} \mathcal{A}(c_\epsilon). \tag{3.10}$$

Since we want to nondimensionalize the elasticity tensor in a unified way, we put the two different dimensionless variants (3.8) and (3.10) in relation to each other and get

$$\tilde{\mathcal{A}}(c_\epsilon) = \sigma_{\mathrm{ref}}^{-1} \mathcal{A}(c_\epsilon) = \sigma_{\mathrm{ref}}^{-1} \varphi_* \tilde{A}(c_\epsilon) =: \kappa \tilde{A}(c_\epsilon). \tag{3.11}$$

In summary, we can state the following dimensionless and scaled system:

$$\begin{aligned} \partial_{\tilde{t}_{\mathrm{d}}} c_\epsilon = \epsilon^r 10^{-r} \tilde{\Delta} \Big(& \tilde{f}'(c_\epsilon) - \epsilon^2 \tilde{\lambda} \tilde{\Delta} c - e'(c_\epsilon) \operatorname{tr}(\tilde{\mathcal{S}}) \\ & + \frac{1}{2} (\mathcal{E}(u_\epsilon) - e(c_\epsilon)\mathbb{1}) : \tilde{\mathcal{A}}'(c_\epsilon)(\mathcal{E}(u_\epsilon) - e(c_\epsilon)\mathbb{1}) \Big), \end{aligned} \tag{3.12a}$$

$$\partial_{\tilde{t}_{\mathrm{m}}}^2 \tilde{u}_\epsilon = \epsilon^s \kappa \tilde{\nabla} \cdot \Big(\tilde{\mathcal{A}}(c_\epsilon) \big(\mathcal{E}(u_\epsilon) - e(c_\epsilon)\mathbb{1}\big) \Big) \tag{3.12b}$$

with a positive dimensionless constant $\kappa := \sigma_{\mathrm{ref}}^{-1} \varphi_*$ that ensures the unification of the dimensionless elasticity tensor in the equations above. The other way around, setting $\tilde{\mathcal{A}}(c_\epsilon) = \kappa^{-1} \tilde{\mathcal{A}}(c_\epsilon)$, of course, could also be chosen.

Special attention must now be paid to the different characteristic times, since they depend on different powers of the scaling parameter ϵ. Further, to represent the diffusion and the mechanics on a common time scale, we need to match the characteristic times and want to unify them as well as possible. Therefore, we require

$$T_{\mathrm{d}} \approx T_{\mathrm{m}} \approx 1. \tag{3.13}$$

For a concrete problem, these conditions allow us to determine r and s. In what follows, we take the extreme cases $r = 2$ and $s = 0$, which correspond to the mechanics being associated with the macroscale and the phase separation associated with the microscale. We show how these numbers arise in the case of the film-balance experiments in Remark 3.1 below.

Dropping the tildes for a simpler notation and better clarity, we get the following dimensionless and scaled system:

$$\begin{aligned} \partial_t c_\epsilon = \epsilon^2 10^{-2} \Delta \Big(& f'(c_\epsilon) - \epsilon^2 \lambda \Delta c - e'(c_\epsilon) \operatorname{tr}(\mathcal{S}) \\ & + \frac{1}{2} (\mathcal{E}(u_\epsilon) - e(c_\epsilon)\mathbb{1}) : \mathcal{A}'(c_\epsilon)(\mathcal{E}(u_\epsilon) - e(c_\epsilon)\mathbb{1}) \Big), \end{aligned} \tag{3.14a}$$

$$\partial_t^2 u_\epsilon = \kappa \nabla \cdot \Big(\mathcal{A}(c_\epsilon) \big(\mathcal{E}(u_\epsilon) - e(c_\epsilon)\mathbb{1}\big) \Big). \tag{3.14b}$$

This system takes the different scales into account by its scaling by exponents of ϵ. Note that so far no assumption has been made about the periodicity of the microstructure, but only about the existence of macroscopic and microscopic characteristic lengths.

Remark 3.1. For the film-balance setup, we choose $L = 1\,\mathrm{m}$ as the characteristic length corresponding to the macroscopic process and $l = 10^{-4}\,\mathrm{m}$ as the characteristic microscopic length scale. Unfortunately, there are currently no complete parameter sets of measured data from experiments available. Within the context of film-balance experiments, a lipid monolayer seems to be a sensitive system and, in the literature, the values of the physical quantities may vary depending on the specific lipid or lipids, the phase state of the monolayer, temperature, and even on the measuring method. However, we are only interested in the orders of magnitude to get an approximate estimate of the characteristic times. Considering typical values of the diffusion coefficient, we choose $1\,\mu\mathrm{m}^2\,\mathrm{s}^{-1}$ as the characteristic value [10]. Hence, we obtain

$$T_{\mathrm{d}} = \frac{10^{-r}\, l^r L^{2-r}}{D_{\mathrm{ref}}} = 10^{-5r+12}.$$

Assuming that one DPPC molecule occupies an area of approximately $1/70 \cdot 10^{-20}\,\mathrm{m}^2$ in the beginning of the phase transition [35] and with the molar mass of DPPC, which is $734.04 \cdot 10^{-3}\,\mathrm{kg\,mol}^{-1}$ [33], we calculate a characteristic value of the order of magnitude $\approx 10^{-2}\,\mathrm{kg\,m}^{-2}$ for the density of a lipid monolayer. With $10^{-1}\,\mathrm{N\,m}^{-1}$ as the characteristic value of the stiffness of a lipid monolayer [34], we get

$$T_{\mathrm{m}} = \left(\frac{l^s L^{2-s} \varrho_{\mathrm{ref}}}{\sigma_{\mathrm{ref}}}\right)^{1/2} = 10^{\frac{1}{2}(-4s-1)},$$

which, with regard to the definition interval of the parameters, leads to $r = 2$ and $s = 0$. Note that, with this scaling, we still consider the mechanics too slow compared to the diffusion, which motivates the quasi-stationary setting in section 5.

4. Periodic homogenization via asymptotic expansions. Using the method of two-scale asymptotic expansions in the context of periodic homogenization [2, 30, 11, 5], we derive an upscaled version of the system (3.14a), (3.14b). We assume the unknowns of (3.14a) and (3.14b) to have an asymptotic expansion in ϵ of the form

$$c_\epsilon(x,t) = \sum_{i=0}^{\infty} \epsilon^i\, c_i(x, x/\epsilon, t) \text{ and } u_\epsilon(x,t) = \sum_{i=0}^{\infty} \epsilon^i\, u_i(x, x/\epsilon, t), \tag{4.1}$$

whereby the coefficient functions c_i and u_i are smooth and these as well as their derivatives are Y-periodic with respect to the second argument, where Y is the representative unit cell of the microscale. We insert the expansions (4.1) into the scaled Cahn–Larché system (3.14a), (3.14b) and identify the coefficients of the different ϵ-powers. This procedure leads to a cascade of partial differential equations.

Generally, for a function $v = v(x,y)$ depending on two variables in the same way as introduced above, we consider $v_\epsilon := v(\cdot, \frac{\cdot}{\epsilon})$, depending only on the variable x. Then, the derivative is given by

$$\frac{\partial}{\partial x_i} v_\epsilon(x) = \frac{\partial}{\partial x_i} v(x, x/\epsilon) + \epsilon^{-1} \frac{\partial}{\partial y_i} v(x, x/\epsilon). \tag{4.2}$$

In what follows, we also write ∇_x and ∇_y for the gradient with respect to x and y, respectively.

For reference in the homogenization process, we first introduce a family of periodic boundary-value problems posed on the unit cell Y, which are known as the cell problems in linear elasticity. For detailed information on these problems, we refer to

[5], where the homogenization result for the equations of linear elasticity was proven using Tartar's method of oscillating test functions. Let $\Omega \subset \mathbb{R}^N$ be a bounded domain and $Y = (0, l_1) \times (0, l_2) \times \cdots \times (0, l_N) \subset \mathbb{R}^N$ with positive numbers $l_1, \dots, l_N$. Let $\mathcal{A} = \mathcal{A}(y)$ with $\mathcal{A} = (a_{ijkh})_{1 \le i,j,k,h \le N}$ being an elliptic fourth-order tensor, and a_{ijkh} being Y-periodic for $i, j, k, h = 1, \dots, N$. For any $l, m \in \{1, \dots, N\}$ we consider the vector-valued function $p^{lm} = (p_k^{lm})_{1 \le k \le N} \in \mathbb{R}^N$ defined by

$$p_k^{lm}(y) := y_m \delta_{kl}, \quad y \in Y, \quad k = 1, \dots, N,$$

with y_m being the mth component of $y \in Y$. Then, for each $l, m = 1, \dots, N$, we want to find a vector-valued function ω^{lm} which solves the following cell problem:

$$\begin{aligned} -\nabla_y \cdot \big(\mathcal{A}\,\mathcal{E}_y(\omega^{lm})\big) &= \nabla_y \cdot \big(\mathcal{A}\,\mathcal{E}_y(p^{lm})\big) \quad \text{in } Y, \\ \omega^{lm} &\quad Y\text{-periodic}. \end{aligned} \tag{4.3}$$

According to the notation used so far, we write $\mathcal{E}_x$ and $\mathcal{E}_y$, where the subscripts indicate the partial derivatives have been taken with respect to the variables x and y, respectively.

We now insert the expansions (4.1) into the system (3.14a), (3.14b) and collect the same powers of ϵ. At scale ϵ^{-2}, provided by the mechanical equation, we obtain

$$\nabla_y \cdot \big(\mathcal{A}(c_0)\,\mathcal{E}_y(u_0)\big) = 0 \quad \text{in } \Omega \times Y \times S. \tag{4.4}$$

Multiplying this equation by u_0 and integrating over Y and by parts yields

$$\int_Y \mathcal{A}(c_0)\,\mathcal{E}_y(u_0) : \mathcal{E}_y(u_0)\,\mathrm{d}y = 0,$$

where the boundary integral vanishes due to the Y-periodicity of the derivatives of u_0 and the components of $\mathcal{A}$. Since $\mathcal{A}$ is positive definite, we get

$$\alpha \,\|\mathcal{E}_y(u_0)\|^2 \le \int_Y \mathcal{A}(c_0)\,\mathcal{E}_y(u_0) : \mathcal{E}_y(u_0)\,\mathrm{d}y = 0$$

for a constant $\alpha > 0$ and which implies $\mathcal{E}_y(u_0) = 0$ and, hence,

$$u_0 = u_0(x, t) \tag{4.5}$$

depends only on the macroscopic variable x and on time. So, we have found a candidate describing the macroscopic deformation. The ϵ^{-1}-term gives

$$\begin{aligned} \nabla_y \cdot \big(\mathcal{A}(c_0)(\mathcal{E}_x(u_0) + \mathcal{E}_y(u_1) - e(c_0)\mathbb{1}) + c_1 \mathcal{A}'(c_0)\mathcal{E}_y(u_0)\big) \\ + \nabla_x \cdot \big(\mathcal{A}(c_0)\mathcal{E}_y(u_0)\big) = 0, \end{aligned} \tag{4.6}$$

which we consider as an equation for the unknown u_1. Using (4.5) and the Y-periodicity of u_1 we get a well-posed problem

$$\begin{aligned} -\nabla_y \cdot \big(\mathcal{A}(c_0)\,(\mathcal{E}_y(u_1) - e(c_0)\mathbb{1})\big) &= \nabla_y \cdot \big(\mathcal{A}(c_0)\,\mathcal{E}_x(u_0)\big) \quad \text{in } \Omega \times Y \times S, \\ u_1 &\quad Y\text{-periodic in } y. \end{aligned} \tag{4.7}$$

For further considerations we need to work with the componentwise representation of this equation, namely,

$$-\sum_{j=1}^{N}\partial_{y_j}\sum_{k,h=1}^{N}\left(a_{ijkh}(c_0)\left(e_{khy}(u_0)-e(c_0)\delta_{kh}\right)\right) = -\sum_{j=1}^{N}\partial_{y_j}\sum_{k,h=1}^{N}\left(a_{ijkh}(c_0)\,e_{khx}(u_0)\right) \tag{4.8}$$

for $i=1,\dots,N$. At this step, we want to gain a representation of $\mathcal{E}_y(u_1)$ in terms of $\mathcal{E}_x(u_0)$. Therefore, we need the auxiliary problems (4.3) for the mechanics, which we also consider now in componentwise form:

$$-\sum_{j=1}^{N}\partial_{y_j}\sum_{k,h}a_{ijkh}(c_0)\,e_{khy}(\omega^{lm}) = \sum_{j=1}^{N}\partial_{y_j}\sum_{k,h}a_{ijkh}(c_0)\,e_{khx}(p^{lm}) \tag{4.9}$$

for $i=1,\dots,N$. Recall that the right-hand side is defined as $(p^{lm}(y))_k = y_m\delta_{kl}$ for $l,m=1,\dots,N$. By using the identity

$$\sum_{k,h=1}^{N}a_{ijkh}(c_0)\,e_{khx}(p^{lm}) = a_{ijlm} \tag{4.10}$$

for $i,j,l,m=1,\dots,N$, we write (4.9) as

$$-\sum_{j=1}^{N}\partial_{y_j}\sum_{k,h}a_{ijkh}(c_0)\,e_{khy}(\omega^{lm}) = \sum_{j=1}^{N}\partial_{y_j}a_{ijlm}(c_0),\quad 1\le i\le N. \tag{4.11}$$

Multiplying both sides of (4.11) with $e_{lmx}(u_0)$ and summing up over l and m yields

$$-\sum_{j=1}^{N}\partial_{y_j}\sum_{k,h=1}^{N}a_{ijkh}(c_0)\sum_{l,m=1}^{N}e_{khy}(\omega^{lm})\,e_{lmx}(u_0) = \sum_{j=1}^{N}\partial_{y_j}\sum_{l,m=1}^{N}a_{ijlm}(c_0)e_{lmx}(u_0) \tag{4.12}$$

for $i=1,\dots,N$. We compare both equations, namely, (4.12) and (4.8) and from the left-hand sides we can directly read off a representation for u_1 in terms of u_0 with the help of the solutions of the cell problems. We obtain

$$e_{ijy}(u_1) = \sum_{l,m=1}^{N}e_{lmx}(u_0)\,e_{ijy}(\omega^{lm}) + e(c_0)\delta_{ij},\quad 1\le i,j\le N. \tag{4.13}$$

Taking into account that $\mathcal{E}_y(u_0) = 0$, the ϵ^0-term leads to

$$\partial_t c_0 = 10^{-2}\Delta_y\Big(f'(c_0) - \lambda\Delta_y c_0 - e'(c_0)\,\mathrm{tr}\left[\mathcal{A}(c_0)(\mathcal{E}_x(u_0) + \mathcal{E}_y(u_1) - e(c_0)\mathbb{1})\right]$$

(4.14a)

$$+\frac{1}{2}(\mathcal{E}_x(u_0) + \mathcal{E}_y(u_1) - e(c_0)\mathbb{1}) : \mathcal{A}'(c_0)\,(\mathcal{E}_x(u_0) + \mathcal{E}_y(u_1) - e(c_0)\mathbb{1})\Big),$$

$$\partial_t^2 u_0 = \kappa\,\nabla_y \cdot \Big(\mathcal{A}(c_0)(\mathcal{E}_x(u_1) + \mathcal{E}_y(u_2) - e'(c_0)c_1\mathbb{1})$$

(4.14b)

$$+ c_1\mathcal{A}'(c_0)(\mathcal{E}_x(u_0) + \mathcal{E}_y(u_1) - e(c_0)\mathbb{1})\Big)$$

$$+\kappa\,\nabla_x \cdot \Big(\mathcal{A}(c_0)(\mathcal{E}_x(u_0) + \mathcal{E}_y(u_1) - e(c_0)\mathbb{1})\Big).$$

Integrating (4.14b) in a componentwise form over Y, we obtain

$$\partial_t^2(u_0)_i = \frac{\kappa}{|Y|}\sum_{j=1}^{N}\partial_{x_j}\int_Y \sum_{k,h=1}^{N} a_{ijkh}(c_0)\left(e_{khx}(u_0) + e_{khy}(u_1) - e(c_0)\delta_{kh}\right)\mathrm{d}y \tag{4.15}$$

for $i = 1,\dots,N$. Thereby, the integral of the first expression of the right-hand side of (4.14b) vanishes due to the Y-periodicity of the involved functions. Next, we insert (4.13), the representation for $\mathcal{E}_y(u_1)$, into (4.15):

$$\partial_t^2(u_0)_i = \frac{\kappa}{|Y|}\sum_{j=1}^{N}\partial_{x_j}\int_Y \sum_{l,m,k,h=1}^{N} a_{ijlm}(c_0)\left(\delta_{lk}\delta_{mh} + e_{lmy}(\omega^{kh})\right)\mathrm{d}y\; e_{khx}(u_0) \tag{4.16}$$

for $i = 1,\dots,N$. In this, we have now found an equation for the macroscopic part of the deformation u_0, which motivates us to define the effective or homogenized elasticity tensor

$$\mathcal{A}^{\mathrm{hom}} = (a^{\mathrm{hom}}_{ijkh})_{1\le i,j,k,h\le N} \tag{4.17}$$

by its components

$$a^{\mathrm{hom}}_{ijkh} := \frac{1}{|Y|}\int_Y \sum_{l,m=1}^{N} a_{ijlm}(c_0)\left(\delta_{lk}\delta_{mh} + e_{lmy}(\omega^{kh})\right)\mathrm{d}y \tag{4.18}$$

for $i,j,k,h = 1,\dots,N$, and write (4.16) as a purely macroscopic equation:

$$\partial_t^2 u_0 = \kappa\nabla_x \cdot \left(\mathcal{A}^{\mathrm{hom}}\,\mathcal{E}_x(u_0)\right) \quad \text{in } \Omega.$$

Furthermore, to use tensor notation for better clarity, we write

$$\mathcal{E}_\omega = \left(e^\omega_{lmkh}\right)_{1\le l,m,k,h\le N} \quad \text{with} \quad e^\omega_{lmkh} = e_{lmy}(\omega^{kh}), \tag{4.19}$$

and we also use the identity tensor

$$\mathcal{I} = \left(\mathcal{I}_{lmkh}\right)_{1\le l,m,k,h\le N} \quad \text{with} \quad \mathcal{I}_{lmkh} = \frac{1}{2}(\delta_{lm}\delta_{kh} + \delta_{mh}\delta_{lk}). \tag{4.20}$$

Now, we can state the formally homogenized system, given by

(4.21a)

$$\partial_t c_0 = 10^{-2}\Delta_y\Big(f'(c_0) - \lambda\Delta_y c_0 - e'(c_0)\,\mathrm{tr}\left[\mathcal{A}(c_0)(\mathcal{I}+\mathcal{E}_\omega)\,\mathcal{E}_x(u_0)\right] + \frac{1}{2}(\mathcal{I}+\mathcal{E}_\omega)\,\mathcal{E}_x(u_0) : \mathcal{A}'(c_0)\,(\mathcal{I}+\mathcal{E}_\omega)\,\mathcal{E}_x(u_0)\Big) \quad \text{in } \Omega\times Y\times S,$$

(4.21b)

$$\partial_t^2 u_0 = \kappa\nabla_x\cdot\left(\mathcal{A}^{\mathrm{hom}}\,\mathcal{E}_x(u_0)\right) \quad \text{in } \Omega\times S.$$

The remaining unknowns of this limit system are c_0 and u_0, the coefficient functions of the first terms of the expansions, whereby only c_0 still depends on the microscopic variable y. The system above is of the so-called distributed-microstructure type. In such a model, a unit cell Y_x is associated with each macroscopic point $x\in\Omega$, in which the local (microscopic) equations are solved, the solutions of which feed into the global (macroscopic) equation after averaging; cf. [1, 31, 32, 11, 19]. In our limit system the local equation (4.21a) for c_0 as well as the cell equations (4.3) have to be solved in every unit cell Y_x and the global equation (4.21b) for u_0 has to be solved in Ω. On Y_x, therefore, a microstructure can be seen which is representative near $x\in\Omega$. In particular, the microstructure can evolve differently at each global point.

Note, that the homogenized tensor depends through c_0 on both variables, on x and on y. Notice further, that the homogenized mechanical equation does not contain the eigenstrain explicitly. Self-generated tensions on the microscale are thus macroscopically averaged out.

We remark that system (4.21) also has an energy associated with it given by

$$\int_{\Omega\times Y} f(c_0) + \frac{\lambda}{2}|\nabla_y c_0|^2 + \frac{1}{2}(\mathcal{I}+\mathcal{E}_\omega)\,\mathcal{E}_x(u_0) : \mathcal{A}(c_0)\,(\mathcal{I}+\mathcal{E}_\omega)\,\mathcal{E}_x(u_0)\,\mathrm{d}y\,\mathrm{d}x, \tag{4.22}$$

which is of similar form to (2.12). Noting that $\mathcal{E}_\omega$ depends on c_0 through (4.13), the gradient-flow structure of the original system is inherited by the limit system.

5. Numerical simulations. We want to test the homogenized system phenomenologically and demonstrate what can be realized with the model by two-dimensional simulations. The implementation was realized using the finite element library FEniCS [17] based on globally continuous, piecewise linear trial and test functions, where the fourth-order equation was taken care of in terms of a mixed finite element method for the concentration and the chemical potential as an auxiliary variable. In order to keep things simple, we take the mechanics as quasi-stationary, i.e., (4.21b) with zero left-hand side; also see Remark 3.1. For discretization in time of the extended Cahn–Hilliard equation (4.21a), we use a fully implicit Euler scheme, where a Newton method is used to solve the resulting algebraic nonlinear system in each time step. For comparison, we accompany the distributed-microstructure Cahn–Larché case studies with numerical simulations of the Cahn–Hilliard equation, nondimensionalized corresponding to section 3, to compare the respective separation process with a separation process without the influence of mechanical stress.

We choose $\Omega=(0,1)^2$ as the macroscopic domain provided with the boundary parts as specified in Figure 1 and a standard unit cell $Y_{x_i}=Y=(0,1)^2$ at each macroscopic point. The macroscopic boundary conditions for the displacement are chosen such that a nonuniform macroscopic strain results. For the displacement, we choose a zero Dirichlet boundary condition on three of the four sides of Ω.

$$u=0 \quad \text{on } (\Gamma_0\cup\Gamma_s)\times S \tag{5.1}$$

and compress the domain at the fourth,

$$u \cdot n = u_g \quad \text{on } \Gamma_g \times S, \tag{5.2}$$

where u_g is chosen such that the macroscopic domain is reduced by 5% in the horizontal direction. A free slip in the tangential direction on $\Gamma_g \times S$ completes the boundary conditions. For c_0, we have periodic boundary conditions and as initial condition we use a locally randomly perturbed constant function, which is Y-periodic in y. More precisely,

$$c_{in}(y) = c_m + \xi(y), \quad y \in Y, \tag{5.3}$$

where ξ is a function drawing random numbers from a uniform distribution in the interval $[-0.005, 0.005)$ for each argument and c_{in} is Y-periodic. In what follows, we consider binodal phase separation by choosing $c_m = 0.3$ in (5.3) as well as spinodal phase separation by setting $c_m = 0.5$. Otherwise, we always take the exact same initial value for all simulations and for c_0 in each Y_{x_i}. The other parameters are always chosen as $\lambda = 10^{-4}$ and $\varphi = 0.75$. For the mechanical parameters, we take the Lamé constants

$$\lambda^\alpha = 0.6, \quad \mu^\alpha = 0.6 \tag{5.4}$$

for the elastically softer phase and

$$\lambda^\beta = 1.2, \quad \mu^\beta = 1.8 \tag{5.5}$$

for the elastically slightly harder phase, so that

$$a^i_{khlm} = \lambda^i \delta_{kh}\delta_{lm} + \mu^i(\delta_{kl}\delta_{hm} + \delta_{km}\delta_{hl}) \tag{5.6}$$

for the components of the elasticity tensors $\mathcal{A}^i$, $i \in \{\alpha, \beta\}$, as well as $e'(c) = 0.2$ unless stated otherwise. In order to realize the micro–macro coupling, at each node x_i of the macroscopic mesh, there is an associated unit cell $Y_{x_i} = Y$ provided with a finer mesh compared with the macroscopic one. For a fixed time step size $\tau > 0$, which is chosen as $\tau = 5 \times 10^{-2}$ in all simulations, we consider the discrete time steps $t_k = t_{k-1} + \tau$ or $t_k = k\tau$ for $k = 1, \dots, k_{max}$ for one $k_{max} \in \mathbb{N}$ and we set $T_{max} := \tau k_{max}$. Then, the solution procedure at each discrete time step t_k works as follows: In each time step, we first solve the cell problems in each unit cell Y_{x_i} associated with each macroscopic node x_i of the macroscopic mesh. With these cell solutions, we assemble and solve the macroscopic equation. Then, with the calculated macroscopic displacement, iterating over each macroscopic node x_i, we solve the evolution equation for the order parameter in every microscopic cell Y_{x_i}.

Figure 2 shows a typical result for the magnitude of the displacement with some marked points of the macroscopic domain in which we show the separation processes in the following simulations. Since we are primarily interested in the microscopic processes and we do not make any comparisons to experiments, we have only chosen a coarse mesh. The microscopic mesh is chosen in such a way that an alignment of the pattern of the evolving microstructure caused by structures of the mesh is avoided and we refer to [8] for studies on such mesh effects.

Our choice of boundary conditions for the displacement implies that the strain tensor varies locally and, in particular, includes shear; see Figure 2. As one can see

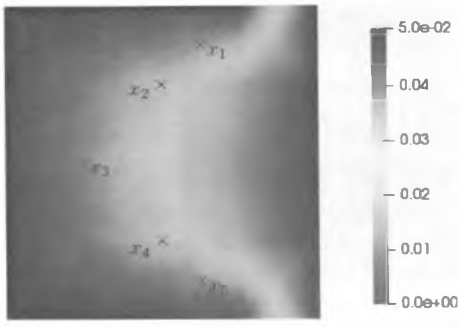

FIG. 2. *Typical magnitude of the macroscopic displacement u_0 and five marked macroscopic points $x_1, \ldots, x_5$.*

from (4.21a), the macroscopic strain $\mathcal{E}(u_0)$ enters in the evolution equation describing the evolving microstructure and, as it may be different in each macroscopic point, the microstructure is expected to be different in each macroscopic point in general. In the following simulations, we therefore expect that the phase separations in the different macroscopic points differ from each other and that an influence on the resulting patterns can be detected.

5.1. Binodal phase separation. In the case of binodal phase separation, we first compare the evolution in time of the separation process described by the distributed-microstructure model in the macroscopic point x_1 with the separation process without elasticity of the corresponding Cahn–Hilliard simulation. Figure 3 shows the results of the Cahn–Hilliard simulation in the left column and the results of the simulation of the distributed-microstructure model in the right column. Plots in one row are at the same point in time t_k specified underneath. For all following simulations of the phase-separation processes, we use the color bar given by Figure 4 for the representation of the order parameter c. Of course, due to the numerical solution methods and modeling aspects, such as the choice of the local free energy, there may be a deviation beyond the limits 0 and 1 for values of the order parameter. However, these are minimal and for standardization we always use this color bar.

The (standard) Cahn–Hilliard simulations show a typical separation process. Regions of pure phases and domains of one component (corresponding to $c = 1$) are formed in the other contiguous phase (corresponding to $c = 0$) and the separation process is quite far advanced already at t_{30}. As time progresses further, the fusion and growth of the domains can be observed, which corresponds to a reduction of the phase boundaries. The shape of the domains corresponds to the energetically favorable circular shape of the red-colored domains. During the fusion of two domains, ellipsoidal structures also occur temporarily, as can be seen particularly well in Figures 3(b) and 3(d), but these quickly relax again into circularly shaped domains.

Considering the results of the DM simulation (we use this abbreviation in what follows for the simulation of the distributed-microstructure model), one can see that the process is roughly the same as that observed by the Cahn–Hilliard simulation. The initially homogeneous mixture separates, regions of pure phases are formed, and the resulting domains of the elastically harder phase merge and grow together.

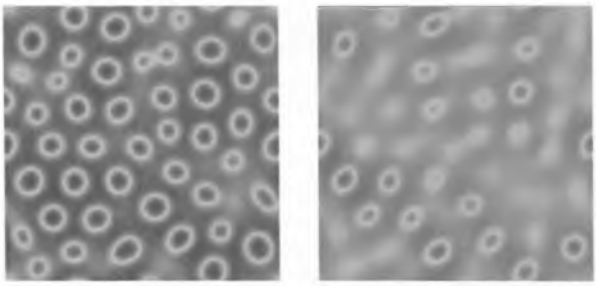

(a) $t_{30} = 1.5$

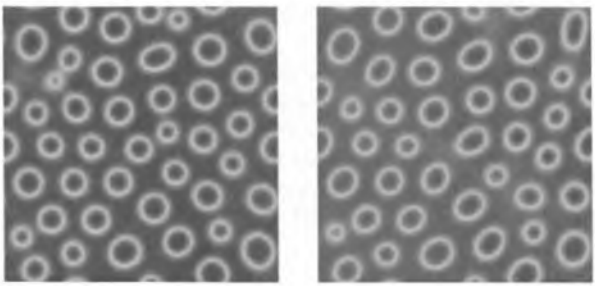

(b) $t_{40} = 2$

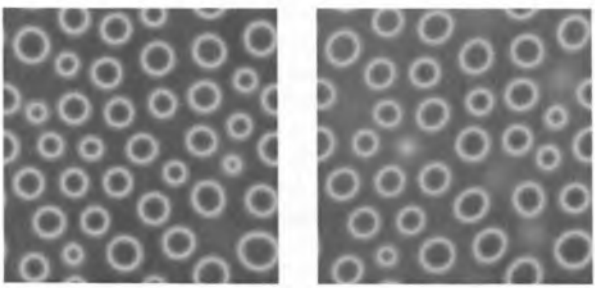

(c) $t_{60} = 3$

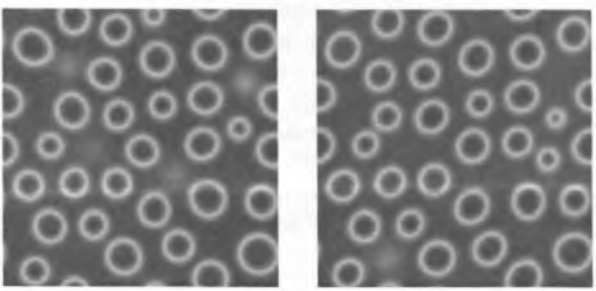

(d) $t_{80} = 4$

FIG. 3. *Pattern of two binodal separation processes at different times t_k; left: results of the Cahn–Hilliard model simulation; right: results of the DM model simulation in the point x_1. The associated color bar is displayed in Figure 4.*

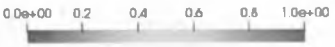

FIG. 4. *Color bar giving values from* 0 *to* 1 *for the visualization of the order parameter* c *in all subsequent figures.*

A comparison of the two separation processes shows that the separation of the phases progresses slowlier in the DM-simulation in x_1 than in the Cahn–Hilliard simulation. This seems to be a general observation in macroscopic points close to the compression boundary Γ_g. Even more significantly, the domains in the DM simulation are ellipsoidally shaped not only during fusion and they are aligned in the diagonal direction from the lower left corner to the upper right corner. The ellipsoid structure is already recognizable from the beginning and is most noticeable in the early stages of the separation process, i.e., immediately with the formation of the domains and can be clearly seen when looking at the emerging microstructure at times t_{30} and t_{40}; cf. Figures 3(a) and 3(b).

The ellipsoidal structure is retained for at least a certain period of time, which can be seen particularly well at times t_{40}, t_{60}, and t_{80} and in comparison to corresponding domains at the same times of the Cahn–Hilliard simulation. In the DM simulation, there are domains which do not grow and remain ellipsoidally shaped during the considered period.

Figure 5 shows patterns in different macroscopic points. The arrangement of the single plots corresponds approximately to the position of the macroscopic points in Ω to which the patterns belong; cf. Figure 2.

As can be seen from the figure, different alignment directions of the domains occur depending on the macroscopic position. The orientation of ellipsoidal domains is most obvious in points x_1 and x_5; see Figures 5(a) and 5(e).

Generally, it can be observed that the orientation direction of the domains in macroscopic points in the upper half of Ω is rather towards the lower left corner and the upper right corner (which corresponds to the points x_1 and x_2), whereas the domains in the macroscopic points of the lower half of Ω are rather oriented towards the upper left corner and the lower right corner (which corresponds to the points x_4 and x_5). In what follows, we refer to these two occurring directions, the two diagonals just described, as orientation diagonals for the alignment of the patterns. While the shear stress in x_2 and x_4 is much smaller than in x_1 and x_5, respectively, it is negligible in the point x_3, which lies in the middle along the vertical coordinate of Ω. Accordingly, the diagonal orientation of the domains in Figures 5(b) and 5(d) is weak but still visible and nonexistent in 5(c). It can also be seen here (and in similar simulations not shown) that there seems to be a preferred direction in which domains merge with other domains. This direction corresponds to the direction of the respective orientation angle of the ellipsoidal domains. These observations fully meet our initial expectations. The macroscopic strain influences the phase separation. It has an effect on the shape and orientation of the domains and the dynamics of the separation process, e.g., merging of domains.

5.2. Spinodal phase separation. The influence of the locally different macroscopic strain becomes more pronounced in the case of spinodal phase separation. Analogously to the binodal case, we first compare the Cahn–Hilliard simulation with the simulation of the separation process in the macroscopic point x_1. The patterns

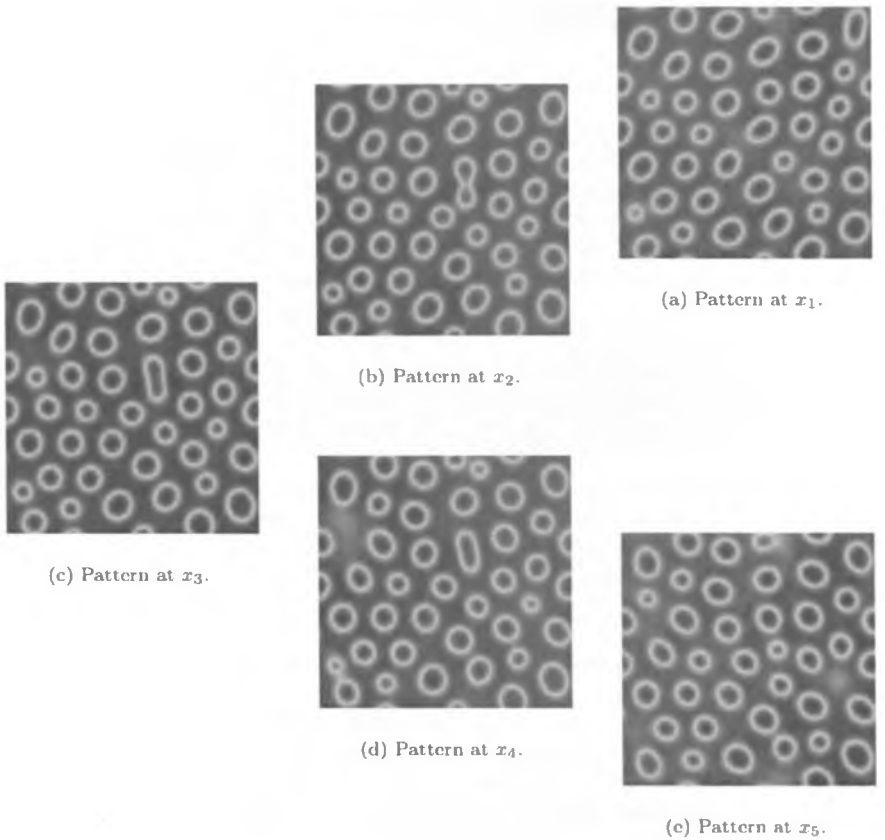

(a) Pattern at x_1.

(b) Pattern at x_2.

(c) Pattern at x_3.

(d) Pattern at x_4.

(e) Pattern at x_5.

FIG. 5. *Pattern of the evolving microstructure in different macroscopic points at time* $t_{10} = 2$ *for binodal phase separation. The associated color bar is displayed in Figure* 4.

at different times can be seen in Figure 6. In the left column of the figure, the results of the Cahn–Hilliard simulation are shown while the solution of the DM simulation can be found in the right column. Results next to each other are at the same times specified underneath. For the comparison of the results from the two simulations, we have chosen different points in time than for the corresponding comparison in the case of binodal separation. The reason for this is that the phase separation is faster here and the selected points in time are adjusted accordingly.

The process of both simulations is roughly the same. In the beginning, the homogeneous mixture separates and regions of pure phases are formed, but in comparison to binodal phase separation, no circular or ellipsoidal domains but stripe-like structures are formed. As time progresses, the regions of pure phases grow, which corresponds to a reduction of the phase boundaries.

At time t_{10}, the phase separation is far from being complete in both cases. At this time, in contrast to the Cahn–Hilliard simulation, in the DM simulation a diagonal orientation of the microstructure is clearly visible already. This difference becomes more pronounced at time t_{20}. The plots of the DM simulation show the diagonal

alignment of the pattern and there are structures which extend diagonally over almost the entire domain. As time progresses, this preferential alignment of the patterns also remains present during the growth of the pure phases as can be seen at times t_{40} and t_{60}. The structure of the pattern becomes more and more similar to diagonal stripes as time progresses. A comparison of Figures 6(b) and 6(d) also shows that the phase boundaries smoothen over time. The patterns of the Cahn–Hilliard simulation, on the other hand, still appear disordered and do not show any particular orientation.

In Figure 7, results for different macroscopic points are shown. The selection of the macroscopic points and the arrangement of the single pictures is the same as in Figure 5 and corresponds approximately to the position of the macroscopic points to which the patterns belong. In spinodal separation, the characteristics of the different orientations of the patterns are more pronounced.

At first glance, it can be said that in all patterns shown in Figure 7 a certain orientation is noticeable in comparison to the corresponding results of the Cahn–Hilliard simulation; cf. Figure 6(d). The observation that we made in the binodal case during the discussion of Figure 5 also applies here, that is that the microstructure in those macroscopic points that is located in the upper or lower half of Ω is oriented along the respective diagonals. However, this orientation is seen much more strongly in the spinodal case. Similarly, the orientation of the patterns in x_1 and x_5 is strongly oriented to the diagonal while the patterns belonging to the points x_2 and x_4 are more vertical already. Located vertically centered in Ω, the formation of the pattern shown in Figure 7(c) is oriented vertically. This becomes particularly clear in comparison to the pattern of the pure Cahn–Hilliard simulation; cf. Figure 6(d).

5.3. Spinodal phase separation with other stiffnesses. Finally, we investigate the effects of a variation of the material stiffness. For this purpose, we consider a weaker and a stiffer material by taking Lamé coefficients multiplied by a factor of one third, i.e., $\lambda^\alpha = 0.2, \mu^\alpha = 0.2$ and $\lambda^\beta = 0.4, \mu^\beta = 0.6$ and taking Lamé coefficients multiplied by a factor of one and two thirds, i.e., $\lambda^\alpha = 1, \mu^\alpha = 1$ and $\lambda^\beta = 2, \mu^\beta = 3$, in comparison to the original choice given in (5.4) and (5.5) and used to produce the results shown so far.

The first row in Figure 8 shows the results of the DM simulation at selected macroscopic points (specified underneath) with the decreased Lamé constants. In the second and the third row, the respective results of the DM simulation with the previously used Lamé constants given by (5.4) and (5.5) and with the increased Lamé constants at the same point in time can be seen. Figures 8(a), 8(d), and 8(g) show patterns in the vertically centered macroscopic point x_3 at time $t_{40} = 2$. In the case of higher Lamé constants, the vertical alignment of the pattern is much more pronounced at this time. On the other hand, the results for the less stiff material given in Figure 8(a), show less vertical alignment and are already similar to the results of a Cahn–Hilliard simulation; see Figure 6(b). Figures 8(b), 8(e), and 8(h) show patterns in x_2, which is located in the upper half of Ω. In the plot of the simulation with the values for elastically harder components, the orientation of the patterns is stronger the stiffer the material. The same applies to the patterns shown in Figures 8(c), 8(f), and 8(i) for the point x_1.

6. Summary and discussion. We considered the Cahn–Larché system in a multiscale context. Assuming two distinct length scales, a microscopic and a macroscopic one, we obtained a Cahn–Larché system in terms of dimensionless quantities, where certain terms were scaled with powers of the ratio of the length scales. For the case where the mechanics is assumed to take place on the macroscopic scale

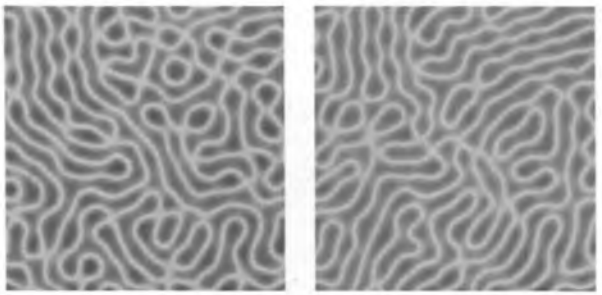

(a) $t_{10} = 0.5$

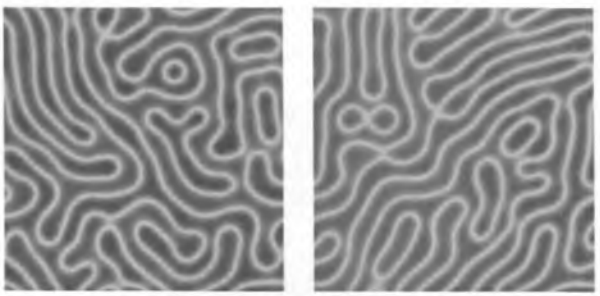

(b) $t_{20} = 1$

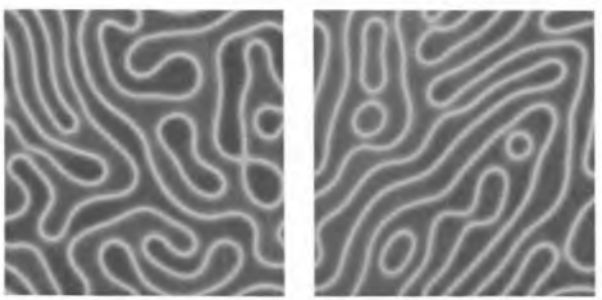

(c) $t_{40} = 2$

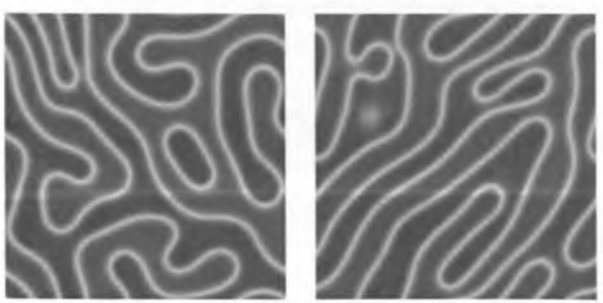

(d) $t_{80} = 4$

FIG. 6. *Pattern of two spinodal separation processes at different times t_k; left: results of the Cahn–Hilliard model simulation; right: results of the DM model simulation in the macroscopic point x_1. The associated color bar is displayed in Figure 4.*

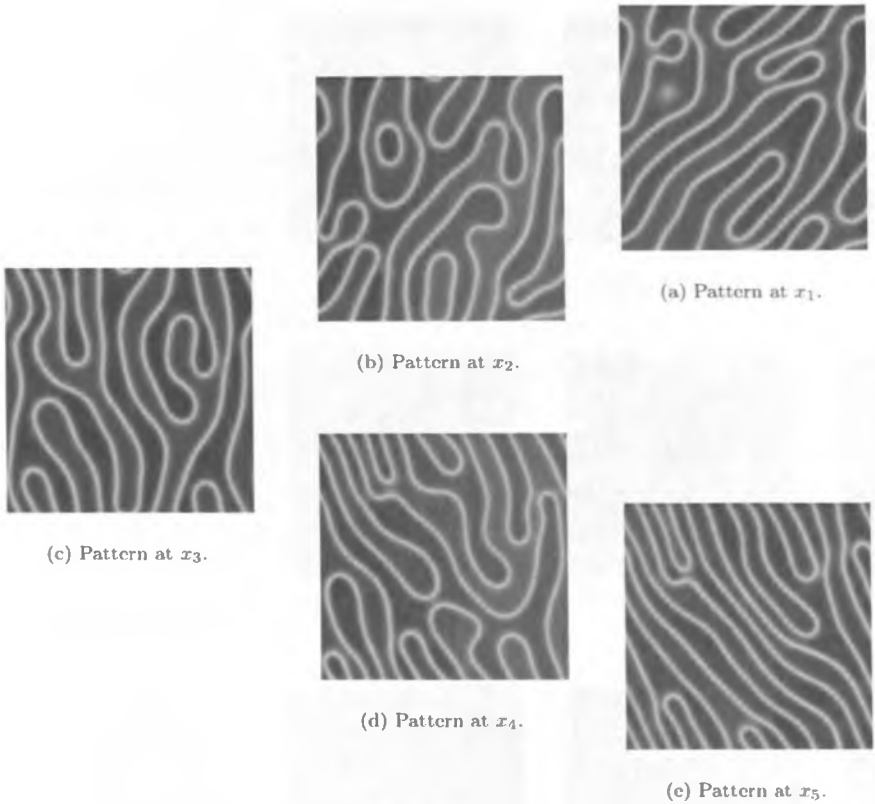

(a) Pattern at x_1.

(b) Pattern at x_2.

(c) Pattern at x_3.

(d) Pattern at x_4.

(e) Pattern at x_5.

FIG. 7. *Pattern of the evolving microstructure at different macroscopic points at time* $t_{80} = 4$ *for spinodal phase separation. The associated color bar is displayed in Figure* 4.

and the separation process occurs on the microscopic scale, which is the case in Langmuir–Blodgett film-balance experiments, we obtained an upscaled system of DM type using the method of asymptotic expansions in a periodic-homogenization setting.

Typical simulation results were presented for the homogenized DM model. As in a single-scale setting, where the separation process is described by the standard Cahn–Larché system, the influence of the mechanics on the patterns can be clearly seen during phase separation. In the DM model, this effect arises on the microscale and it is particularly evident in the spinodal case. In the binodal case, ellipsoidal shapes were seen particularly clearly during the early stage of phase separation. Over time, it could be observed that the ellipsoidal shapes relax into more circular shapes. In contrast, in the case of spinodal separation, we found that the alignment of the patterns due to elastic stresses becomes clearer and stricter as time progresses. Furthermore, these effects appear more strongly with elastically harder material parameters. Nevertheless, in all cases, a certain alignment of the microstructure can be seen, which varies locally macroscopically and which is in line with our expectations regarding the model.

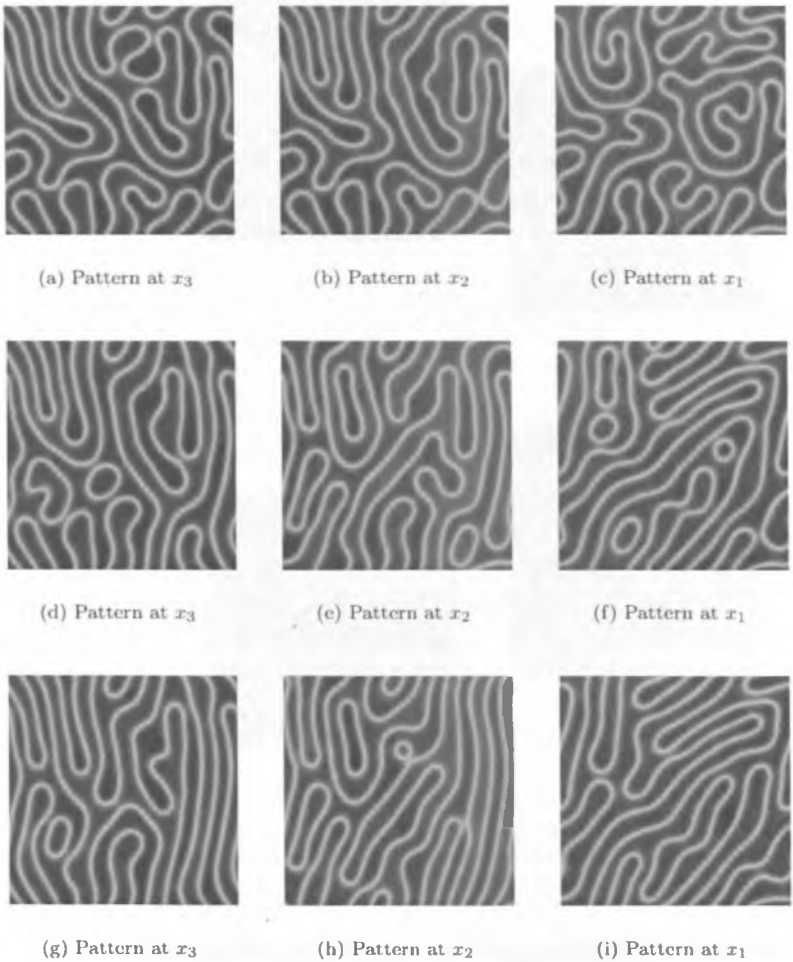

FIG. 8. *Patterns at different macroscopic points at time $t_{40} = 2$ for elastically weaker (top row) and stiffer (bottom row) materials. The associated color bar is displayed in Figure 4.*

Unfortunately, no quantitative measurements of the film-balance experiments, which motivated the developed multiscale model, are available. A quantitative comparison with numerical simulations is required in the future to validate the limit model. Since the mathematics has been kept general, an application in three dimensions is also feasible. For example, models of evolving microstructures in phase-separating metal alloys under macroscopic mechanical stress could be considered in an analogous fashion. Furthermore, the upscaling method based on matched asymptotic expansions is mathematically heuristic. From an analytic point of view, passing to the limit in a mathematically rigorous way would be an important mathematical justification of the limit model. This poses a number of challenges, however, owing to the multiple nonlinearities and the ϵ^2-scaling.

REFERENCES

[1] T. Arbogast, J. Douglas Jr., and U. Hornung, *Derivation of the double porosity model of single phase flow via homogenization theory*, SIAM J. Math. Anal., 21 (1990), pp. 823–863.

[2] A. Bensoussan, J.-L. Lions, and G. Papanicolaou, *Asymptotic analysis for periodic structures*, North-Holland, Amsterdam, 1978.

[3] O. Boyarkin, S. Burger, T. Franke, T. Fraunholz, R. H. W. Hoppe, S. Kirschler, K. Lindner, M. A. Peter, F. G. Strobl, and A. Wixforth, *Transport at interfaces in lipid membranes and enantiomer separation*, in Transport Processes at Fluidic Interfaces, D. Bothe and A. Reusken, eds., Springer, Cham, Switzerland, 2017, pp. 489–530, https://doi.org/10.1007/978-3-319-56602-3_17.

[4] S. Burger, T. Fraunholz, C. Leirer, R. H. W. Hoppe, A. Wixforth, M. A. Peter, and T. Franke, *Comparative study of the dynamics of lipid membrane phase decomposition in experiment and simulation*, Langmuir, 29 (2013), pp. 7565–7570.

[5] D. Cioranescu and P. Donato, *An Introduction to Homogenization*, Oxford Lecture Ser. Math. Appl., Oxford University Press, Oxford, 1999.

[6] J. Eshelby, *Elastic inclusions and inhomogeneities*, in Progress in Solid Mechanics, Vol. 2, North Holland, Amsterdam, 1961, pp. 89–140.

[7] P. Fratzl, O. Penrose, and J. Lebowitz, *Modeling of phase separation in alloys with coherent elastic misfit*, J. Stat. Phys., 95 (1999), pp. 1429–1503.

[8] T. Fraunholz, *Transport at Interfaces in Lipid Membranes and Enantiomer Separation*, PhD thesis, Universität Augsburg, Augsburg, Germany, 2014, https://opus.bibliothek.uni-augsburg.de/opus4/frontdoor/index/index/docId/3067.

[9] H. Garcke, *On Mathematical Models for Phase Separation in Elastically Stressed Solids*, Habilitation thesis, Universität Bonn, Bonn, Germany, 2000.

[10] M. Gudmand, M. Fidorra, T. Bjornholm, and T. Heimburg, *Diffusion and partitioning of fluorescent lipid probes in phospholipid monolayers*, Biophys. J., 96 (2009), pp. 4598–4609, https://doi.org/10.1016/j.bpj.2009.01.063.

[11] U. Hornung, ed., *Homogenization and Porous Media*, Springer, New York, 1997.

[12] A. Khachaturyan, *Some questions concerning the theory of phase transformations in solids*, Sov. Phys. Solid State, 8 (1967), pp. 2163–2168.

[13] K. Klopfer and T. Vanderlick, *Isotherms of dipalmitoylphosphatidylcholine (DPPC) monolayers: Features revealed and features obscured*, J. Colloid Interface Sci., 182 (1996), pp. 220–229.

[14] P. Krüger and M. Lösche, *Molecular chirality and domain shapes in lipid monolayers on aqueous surfaces*, Phys. Rev. E(3), 62 (2000), pp. 7031–7043, https://doi.org/10.1103/PhysRevE.62.7031.

[15] T. Küpper and N. Masbaum, *Simulations of particle growth and Ostwald, ripening via Cahn–Hilliard equation*, Acta Metall. Mater., 42 (1994), pp. 1847–1858.

[16] F. Larché and J. Cahn, *The effect of self-stress on diffusion in solids*, Acta Metall., 30 (1982), pp. 1835–1845.

[17] A. Logg, K.-A. Mardal, and G. N. Wells, eds., *Automated Solution of Differential Equations by the Finite Element Method*, Springer, Berlin, 2012.

[18] C. McConlogue and T. Vanderlick, *A close look at domain formation in DPPC monolayers*, Langmuir, 13 (1997), pp. 7158–7164.

[19] S. A. Meier, *Two-Scale Models for Reactive Transport and Evolving Microstructure*, PhD thesis, Universität Bremen, Bremen, Germany, 2008.

[20] T. Merkle, *The Cahn–Larché System: A Model for Spinodal Decomposition in Eutectic Solder – Modelling, Analysis and Simulation*, PhD thesis, Universität Stuttgart, Stuttgart, Germany, 2005.

[21] A. Miller and H. Möhwald, *Diffusion limited growth of crystalline domains in phospholipid monolayers*, J. Chem. Phys., 86 (1987), pp. 4258–4265, https://doi.org/10.1063/1.451886.

[22] A. Miranville, *The Cahn–Hilliard Equation: Recent Advances and Applications*, CBMS-NSF Regional Conf. Ser. Appl. Math., SIAM, Philadelphia, 2019.

[23] H. Möhwald, *Phospholipid monolayers*, in Structure and Dynamics of Membranes, R. Lipowsky and E. Sackmann, eds., Handb. Biol. Phys. 1, North-Holland, Amsterdam, 1995, pp. 161–211, https://doi.org/10.1016/S1383-8121(06)80021-7.

[24] T. Mura, *General theory of eigenstrains*, in Micromechanics of Defects in Solids, Springer, 1987, Dordrecht, The Netherlands, pp. 1–73, https://doi.org/10.1007/978-94-009-3489-4_1.

[25] K. Nag, C. Boland, N. Rich, and K. Keough, *Epifluorescence microscopic observation of monolayers of dipalmitoylphosphatidylcholine: dependence of domain size on compression rates*, Biochem. Biophys. Acta., 1068 (1991), pp. 157–160.

[26] M. Panfilov, *Macroscale Models of Flow Through Highly Heterogeneous Porous Media*. Kluwer Academic, Dordrecht, The Netherlands, 2000.

[27] M. A. Peter and M. Böhm, *Scalings in homogenisation of reaction, diffusion and interfacial exchange in a two-phase medium*, in Proceedings of Equadiff 11, International Conference on Differential Equations. M. Fila. A. Handlovicova, K. Mikula, M. Medved, P. Quittner. and D. Sevcovic, eds., Comenius University, Bratislava, Slovakia, 2005, pp. 369–376, http://www.iam.fmph.uniba.sk/equadiff/html/_proceedings/_peter/peter.pdf.

[28] M. A. Peter and M. Böhm, *Different choises of scaling in homogenization of diffusion and interfacial exchange in a porous medium*, Math. Methods Appl. Sci., 31 (2008), pp. 1257–1282.

[29] M. A. Peter and M. Böhm, *Multiscale modeling of chemical degradation mechanisms in porous media with evolving microstructure*, Multiscale Model. Simul., 7 (2009), pp. 1643–1668, https://doi.org/10.1137/070706410.

[30] E. Sánchez-Palencia, *Non-homogeneous media and vibration theory*, Lecture Notes in Phys. 127, Springer, Berlin, 1980.

[31] R. E. Showalter, *Diffusion models with microstructure*, Transp. Porous Media, 6 (1991), pp. 567–580, https://doi.org/10.1007/BF00137850.

[32] R. E. Showalter, *Distributed microstructure models of porous media*, in Flow in Porous Media: Proceedings of the Oberwolfach Conference, June 21–27, 1992, J. Douglas Jr. and U. Hornung, eds., Birkhäuser, Basel. 1993, pp. 155–163, https://doi.org/10.1007/978-3-0348-8564-5_14.

[33] Sigma-Aldrich, *Data of DPPC*, 2019, https://www.sigmaaldrich.com/catalog/product/avanti/850355c.

[34] D. Steppich, *Kopplung von mechanischen und thermodynamischen Eigenschaften von Phospholipidmembranen in der Nähe von Phasenumwandlungen – Bedeutung für Anwendungen und Biologie*, diploma thesis, Universität Augsburg, Augsburg, Germany, 2005.

[35] P. Toimil, X. Prieto, J. Miñones, and F. Sarmiento, *A comparative study of f-DPPC/DPPC mixed monolayers. influence of subphase temperature on f-DPPC and DPPC monolayers*, Phys. Chem. Chem. Phys., 12 (2010), pp. 13323–13332, https://doi.org/10.1039/c0cp00506a.

[36] U. Weikard, *Numerische Lösungen der Cahn-Hilliard-Gleichung und der Cahn-Larché-Gleichung*, Ph.D thesis, Rheinische Friedrich-Wilhelms-Universität Bonn, Bonn, Germany, 2002.